Implicit Electromagnetic Simulation

J.N. Leboeuf

Institute for Fusion Studies

The University of Texas at Austin

Austin, Texas 78712-1060

Abstract
ω Greek omega
Δt Greek capital delta, t

Introduction Ω_α Greek capital omega, sub Greek alpha

Section II
x_j position x, sub j
v_j velocity v, sub j
∇ inverted Greek capital delta
ρ Greek rho
γ_α Greek gamma, sub Greek alpha
δ Greek delta
$\mathcal{L}$ Calligraphic L
χ Greek capital chi
ϵ Greek epsilon
$\mathcal{F}$ Calligraphic F
$\mathcal{P}$ Calligraphic P
$\perp$ sub perpendicular
$\parallel$ sub parallel
$\mathcal{M}$ Calligraphic M

Section III
c speed of light c
v_T velocity v, sub capital T
ϕ Greek phi
κ_B Greek kappa, sub capital B
π Greek pi
ν Greek nu

Abstract

A direct method for the implicit particle simulation of electromagnetic phenomena in magnetized, multi-dimensional plasmas is developed. The method is second-order accurate for $\omega\Delta t < 1$, with ω a characteristic frequency and time step Δt. Direct time integration of the implicit equations with simplified space differencing allows the consistent inclusion of finite particle size. Decentered time differencing of the Lorentz force permits the efficient simulation of strongly magnetized plasmas. A Fourier-space iterative technique for solving the implicit field corrector equation, based on the separation of plasma responses perpendicular and parallel to the magnetic field and longitudinal and transverse to the wavevector, is described. Wave propagation properties in a uniform plasma are in excellent agreement with theoretical expectations. Applications to collisionless tearing and coalescence instabilities further demonstrate the usefulness of the algorithm.

I. Introduction

We describe an algorithm for the efficient simulation of low frequency phenomena in a magnetically-confined, collisionless plasma. Examples of possible applications are, kinetic modifications of MHD waves and instabilities, collisionless tearing modes, and radio frequency (RF) plasma heating or current drive at low frequencies. These applications are distinguished by characteristic frequency (mode frequency) ω much smaller than the plasma frequency ω_α or cyclotron frequency Ω_α for one or several species $\alpha(\omega \ll \omega_\alpha,\ \Omega_\alpha)$.

In contrast to single or multiple fluid plasma simulation methods[1] which efficiently represent confined plasma phenomena on very long time scales by moment equations, the algorithm described here follows individual particle orbits, and thus retains all low-frequency kinetic effects.

The algorithm differs from conventional (explicit) particle simulation methods,[2] which are appropriate for short time scale phenomena. In contrast to these methods, for which the maximum allowable time step Δt is limited to multiples of ω_α^{-1} or Ω_α^{-1}, a direct implicit treatment of the particle and field equations allows much larger time steps to be used. The implicit treatment removes the explicit stability condition without significantly affecting the low-frequency modes of the system.

The possibility of using implicit field computations for particle simulation was considered some time ago,[3] and it was concluded that a direct inversion of the implicit particle difference equations was impractical. Mason[4] showed that including only the cold fluid contribution in the time-advanced plasma response was sufficient for stability. An alternative to this moment-implicit method is the direct implicit method.[5–9] The moment method has been applied to two-dimensional electromagnetic plasma simulation[10] and the direct method has been applied to two-dimensional electrostatic plasma simulation,[11] and recently, to two-dimensional electromagnetic plasma simulation.[12]

The algorithm described here extends the earlier electrostatic formulation[11] to the electromagnetic case. The improvements previously implemented are thus applicable to electromagnetic simulations. The method is second-order accurate for small $\omega\Delta t$, with associated reduced damping of these low-frequency modes compared to first-order schemes. Direct time integration of the implicit equations with simplified spatial differ-

encing allows the consistent inclusion of finite particle size, so that long-wavelength modes are accurately represented with relatively few particles per cell. Decentered time differencing of the Lorentz force[11] permits the efficient simulation of strongly magnetized plasmas ($\Omega_\alpha \Delta t \gg 1$). An iterative technique for solving the implicit field corrector equation is described. It[13,14] separates the plasma response into parts parallel and perpendicular to the magnetic field, and separates the longitudinal and transverse parts of the response. Then an approximate inverse for each of these parts is obtained and the results selectively combined to give a rapidly convergent method. These manipulations are done in Fourier space.

The algorithm has been implemented in bounded as well as periodic configurations. Wave propagation properties in a uniform plasma have been thoroughly tested. Applications of the algorithm to collisionless tearing and coalescence instabilities have also been carried out.

This paper is organized as follows. In Sec. II, our direct implicit electromagnetic algorithm is described. The dispersion and fluctuation properties of the algorithm are demonstrated in Sec. III. Applications to collisionless tearing and coalescence are given in Sec. IV, while Sec. V is devoted to a summary and discussion of the algorithm and its results.

II. Direct Implicit Electromagnetic Algorithm

The collisionless interaction of a non-relativistic plasma of finite sized simulation particles is described by Newton's equations of motion. Single particle forces are given by the Lorentz force due to the electromagnetic fields. The resulting finite sized particle equations (in MKS units) are

$$\dot{\mathbf{x}}_j = \mathbf{v}_j, \tag{2.1a}$$

$$\dot{\mathbf{v}}_j = \mathbf{A}_\alpha(\mathbf{x}_j, t) + \mathbf{v}_j \times \mathbf{\Omega}_\alpha(\mathbf{x}_j, t), \tag{2.1b}$$

for a large number of simulation particles of each species $\alpha = e, i$; $j = 1, 2, \ldots, N_0$. The over dot in Eq. (2.1) represents differentiation with respect to the time t.

In Eq. (2.1), the electric acceleration is

$$\mathbf{A}_\alpha = \left(\frac{q}{m}\right)_\alpha H{*}\mathbf{E}, \tag{2.2}$$

where q_α, m_α are the single particle charge and mass for species α and $\mathbf{E}$ is the electric field. It is assumed that $q_i = -q_e$. The convolution operator H^*, appearing in Eq. (2.2) represents sampling of the field by the finite sized charge cloud of the simulation particle. Thus,

$$(H{*}\mathbf{E})(\mathbf{x}) = \int d\mathbf{x}' h(\mathbf{x} - \mathbf{x}')\mathbf{E}(\mathbf{x}'), \tag{2.3}$$

where h is an interpolation function satisfying $\int d\mathbf{x}' h(\mathbf{x} - \mathbf{x}') = 1$ and the integrals are over the whole domain.

The cyclotron frequency (vector) $\mathbf{\Omega}_\alpha$ of Eq. (2.1) is given in a similar fashion as

$$\mathbf{\Omega}_\alpha = \left(\frac{q}{m}\right)_\alpha H{*}\mathbf{B}, \tag{2.4}$$

where $\mathbf{B}$ is the magnetic induction.

Field quantities evolve according to the Maxwell equations with self-consistent sources given by the particles. The relevant equations are Faraday's law

$$\frac{\partial \mathbf{B}}{\partial t} = -\nabla \times \mathbf{E}, \tag{2.5}$$

and Ampere's law

$$\frac{\partial \mathbf{E}}{\partial t} = c^2 \left(\nabla \times \mathbf{B} - \mu_0 \mathbf{J} \right). \tag{2.6}$$

In Eq. (2.6), c is the velocity of light and μ_0 the permeability of free space, and the current $\mathbf{J}$ is determined from the particle data as

$$\mathbf{J}(\mathbf{x}) = \sum_j q_\alpha h(\mathbf{x} - \mathbf{x}_j) \mathbf{v}_j. \tag{2.7}$$

As a consequence of Ampere's law and Gauss' law, total charge is conserved

$$\frac{\partial \rho}{\partial t} + \nabla \cdot \mathbf{J} = 0, \tag{2.8}$$

where the charge density ρ is given from the particle data

$$\rho(\mathbf{x}) = \sum_j q_\alpha h(\mathbf{x} - \mathbf{x}_j). \tag{2.9}$$

As is usual in particle simulations, the differential equations of this section are solved by introducing a spatial mesh and discretizing all quantities with respect to time. A set of time marching difference equations is developed and used to advance the particle and field data.

A set of (time) explicit difference equations is obtained by applying the usual leap-frog differencing to Eq. (2.1). It is convenient to introduce normalized variables. Let Δ be the spatial mesh spacing, assumed uniform and the same in all dimensions, for simplicity. Let Δt be the time step and denote time levels by a superscript. Then, the leap-frog difference equations for Eq. 2.1 may be written as

$$\hat{\mathbf{x}}_j^{n+1} = \hat{\mathbf{x}}_j^n + \hat{\mathbf{v}}_j^{n+1/2}, \tag{2.10a}$$

$$\hat{\mathbf{v}}_j^{n+1/2} = \hat{\mathbf{v}}_j^{n-1/2} + \hat{\mathbf{A}}_\alpha^n(\hat{\mathbf{x}}_j^n) + \frac{1}{2}\left[(1+\gamma_\alpha)\hat{\mathbf{v}}_j^{n+1/2} + (1-\gamma_\alpha)\hat{\mathbf{v}}_j^{n-1/2}\right] \times \hat{\mathbf{\Omega}}_\alpha^n(\hat{\mathbf{x}}_j^n). \tag{2.10b}$$

In Eq. (2.10), the normalized quantities are given by

$$\hat{\mathbf{x}}_j = \mathbf{x}_j/\Delta, \tag{2.11a}$$

$$\hat{\mathbf{v}}_j = \mathbf{v}_j \Delta t/\Delta, \tag{2.11b}$$

$$\hat{\mathbf{A}}_\alpha = \left(\frac{q}{m}\right)_\alpha \frac{(\Delta t)^2}{\Delta} H * \mathbf{E}, \tag{2.11c}$$

$$\hat{\mathbf{\Omega}}_\alpha = \left(\frac{q}{m}\right)_\alpha \Delta t H * \mathbf{B}, \tag{2.11d}$$

and γ_α is a centering parameter. In applications where $\hat{\Omega}_\alpha \lesssim 1$, $\gamma_\alpha = 0$ may be chosen and the full cyclotron motion of species α is followed with the resulting time-centered equation. For $\hat{\Omega}_\alpha \gg 1$, $\gamma_\alpha > 0$ gives damping of the cyclotron motion. The resulting difference equations describe the zero-gyroradius, low-frequency motion of species α.[11]

The convolution operators of Eqs. (2.11c) and (2.11d) are approximated by an interpolation from the mesh in the usual way,

$$(H*E)(\hat{\mathbf{x}}\Delta) = \sum_{\mathbf{m}} i(\hat{\mathbf{x}} - \mathbf{m})(H*\mathbf{E})(\mathbf{m}\Delta). \tag{2.12}$$

In Eq. (2.12), $\mathbf{m} = (m_1, m_2)$ is a multi-integer labelling mesh points and i is an interpolation function which is local so that the sum contains but a few terms and is thus easily evaluated.

Next, consider the differencing of the field equations. It is convenient to adopt a leap-frog scheme for the field quantities also. Thus, the difference approximation of Eqs. (2.5) and (2.6) may be written as

$$\hat{\mathbf{B}}^{n+1/2} = \hat{\mathbf{B}}^{n-1/2} - \hat{\nabla} \times \hat{\mathbf{E}}^n, \tag{2.13a}$$

$$\hat{\mathbf{E}}^{n+1} = \hat{\mathbf{E}}^n + \hat{c}^2 \hat{\nabla} \times \hat{\mathbf{B}}^{n+1/2} - f_n H^2{}_* \hat{\mathbf{J}}^{n+1/2}, \tag{2.13b}$$

with the normalized quantities are,

$$\hat{\mathbf{E}}^n = \hat{\mathbf{A}}_e^n, \tag{2.14a}$$

$$\hat{\mathbf{B}}^{n+1/2} = \hat{\mathbf{\Omega}}_e^{n+1/2}, \tag{2.14b}$$

$$\hat{c}^2 = \left(\frac{c\Delta t}{\Delta}\right)^2, \tag{2.14c}$$

$$\hat{\nabla} = \Delta \nabla, \tag{2.14d}$$

$$\hat{\mathbf{J}}^{n+1/2}(\mathbf{m}) = \frac{1}{2} \sum_j \pm \left[i(\mathbf{m} - \hat{\mathbf{x}}_j^n) + i(\mathbf{m} - \hat{\mathbf{x}}_j^{n+1}) \right] \hat{\mathbf{v}}_j^{n+1/2}, \tag{2.14e}$$

and

$$f_n = \frac{N_x \times N_y}{N_0} (\hat{\Delta} t)^2. \tag{2.14f}$$

In Eq. (2.14e), the upper (lower) sign is chosen for electrons (ions). In Eq. (2.14f), N_x, N_y are the number of cells in the x, y directions and N_0, as noted earlier, the number

of particles of either species. The normalized time step is given by $\hat{\Delta}t = \omega_{e0}\Delta t$, where ω_{e0} is the mean electron plasma frequency corresponding to the number density obtained from the total electron inventory and the total volume.

Because of truncation errors, conservation of charge demanded by Eq. (2.8) will not be exact.[15] To prevent the accumulation of these errors, the electric field $\hat{E}^{n+1}$ appearing in Eq. (2.13b) is replaced by $\hat{\mathbf{E}}'^{n+1} = \hat{\mathbf{E}}^{n+1} + \nabla\psi$ where

$$\hat{\nabla}^2\psi = \nabla\cdot\mathbf{E}'^{n+1} - f_n H^2 * \hat{\rho}^{n+1}, \tag{2.15}$$

with the normalized density

$$\hat{\rho}^n(\mathbf{m}) = \sum_j \pm i(\mathbf{m} - \hat{\mathbf{x}}_j). \tag{2.16}$$

In this way, the finite difference form of Gauss' law is exactly satisfied; that is,

$$\boldsymbol{\nabla}\cdot\hat{\mathbf{E}}^{n+1} = f_n H^2 * \hat{\rho}^{n+1}. \tag{2.17}$$

In the subsequent discussion, the carats written to indicate normalized quantities are suppressed. It is understood (unless stated otherwise) that all quantities are normalized as indicated previously. The explicit difference scheme consists of Eq. (2.10) for advancing the particles, Eq. (2.13) for advancing the fields, and Eqs. (2.14e), (2.15), and (2.16) for determining the source, $\mathbf{J}^{n+1/2}$, for the field advance. Particle pushing requires the quantities $\mathbf{A}_\alpha^n$, $\boldsymbol{\Omega}_\alpha^n$ and these are given by

$$\mathbf{A}_e^n = E^n, \tag{2.18a}$$

$$\mathbf{A}_i^n = -\frac{m_e}{m_i}\mathbf{E}^n, \tag{2.18b}$$

$$\boldsymbol{\Omega}_e^n = \frac{1}{2}\left(\mathbf{B}^{n-1/2} + \mathbf{B}^{n+1/2}\right), \tag{2.18c}$$

and

$$\boldsymbol{\Omega}_i^n = -\frac{m_e}{m_i}\boldsymbol{\Omega}_e^n. \tag{2.18d}$$

This explicit scheme imposes several restrictions on the time step. Electron plasma oscillations require $\Delta t < 1$. Additionally, electromagnetic (light) wave propagation requires

$k_{\max}c < 1$, where $k_{\max}$ is the largest allowed wavenumber. These conditions impose very severe limitations on the study of low-frequency electromagnetic phenomena, which require many thousands of such small time steps to develop. If the explicit equations are modified by including time-advanced fields in the particle acceleration (making the resulting equations implicit) these time step restrictions are avoided.

The electromagnetic implicit method is an extension of earlier work on the electrostatic magnetized plasma.[11] The electric field used to accelerate the particles is replaced by a time-filtered electric field which contains time-advanced information. This removes the constraint associated with the electron plasma oscillations. The Courant condition associated with the propagation of light waves is also removed by introducing time-filtered information into the field advance equations. In contrast to Langdon,[16] time-filtering is introduced into Ampere's law rather than into Faraday's law. In this way, the magnetic field advance remains completed explicit, and the **B**-field at time n needed to advance the particles does not need to be estimated from an implicit prediction. This has the important effect that there are no terms arising in the plasma response from the variation of $\mathbf{B}^n$ with the time advanced electric field.

The implicit electromagnetic particle and field equations to be considered are

$$\mathbf{x}_j^{n+1} = \mathbf{x}_j^n + \mathbf{v}_j^{n+1/2}, \tag{2.19a}$$

$$\mathbf{v}_j^{n+1/2} = \mathbf{v}_j^{n-1/2} + \bar{\mathbf{A}}_\alpha^n(\mathbf{x}_j^n) + \frac{1}{2}\left[(1+\gamma_\alpha)\mathbf{v}_j^{n+1/2} + (1-\gamma_\alpha)\mathbf{v}_j^{n-1/2}\right] \times \mathbf{\Omega}_\alpha^n(\mathbf{x}_j^n), \tag{2.19b}$$

$$\mathbf{J}^{n+1/2}(\mathbf{m}) = \frac{1}{2}\sum_j \pm\left[i(\mathbf{m}-\mathbf{x}_j^n) + i(\mathbf{m}-\mathbf{x}_j^{n+1})\right]\mathbf{v}_j^{n+1/2}, \tag{2.19c}$$

$$\rho^{n+1}(\mathbf{m}) = \sum_j \pm i\left(\mathbf{m}-\mathbf{x}_j^{n+1}\right), \tag{2.19d}$$

$$\mathbf{B}^{n+1/2} = \mathbf{B}^{n-1/2} - \nabla\times\mathbf{E}^n, \tag{2.19e}$$

$$\mathbf{E}'^{n+1} = \mathbf{E}^n + c^2\nabla\times\bar{\mathbf{B}}^{n+1/2} - f_n H^2 * J^{n+1/2}, \tag{2.19f}$$

$$\mathbf{E}^{n+1} = \mathbf{E}'^{n+1} - \nabla\psi, \tag{2.19g}$$

$$\nabla^2\psi = \nabla\cdot\mathbf{E}'^{n+1} - f_n H^2 * \rho^{n+1}, \tag{2.19h}$$

$$\bar{\mathbf{A}}_e^n = \bar{\mathbf{E}}^n, \tag{2.19i}$$

$$\bar{\mathbf{A}}_i^n = -\frac{m_e}{m_i}\bar{\mathbf{E}}^n, \tag{2.19j}$$

$$\mathbf{\Omega}_e^n = \frac{1}{2}\left[\mathbf{B}^{n+1/2} + \mathbf{B}^{n-1/2}\right], \tag{2.19k}$$

$$\mathbf{\Omega}_i^n = \frac{m_e}{m_i}\mathbf{\Omega}_e^n, \tag{2.19l}$$

$$\bar{\mathbf{E}}^n = \frac{1}{2}\left[\mathbf{E}^{n+1} + \bar{\mathbf{E}}^{n-1}\right], \tag{2.19m}$$

and

$$\bar{\mathbf{B}}^{n+1/2} = \frac{1}{2}\left[\mathbf{B}^{n+3/2} + \bar{\mathbf{B}}^{n-1/2}\right]. \tag{2.19n}$$

These implicit equations cannot be solved directly. Either additional information about higher moments needs to be introduced[4,10] or a predictor-corrector method can be developed which directly expresses the plasma response to the time advanced electric field. The latter "direct" method[6,11,12] is chosen here. For this, the particles are pushed at least twice. First, a prediction is made by pushing the particles using some guess for the unknown, time-advanced field. The error in satisfying the implicit field equation is computed. A field adjustment is computed in which the plasma response is estimated from the particle equations of motion. Then a correction to the particle data is made by again pushing the particles with the corrected electric field. While this iteration could be repeated with further field corrections, it has not been found necessary to use more than one corrector pass.

Application of this method gives the following algorithm. First, approximate $\mathbf{E}^{n+1}$ by $\tilde{\mathbf{E}} \equiv \bar{\mathbf{E}}^{n-1}$. Then all of Eqs. (2.19) except Eq. (2.19f) may be stepped forward in time. Denote the resulting quantities by writing them with a "tilde". There will be some error in the remaining equation. Define the error $\boldsymbol{\epsilon}^n$ by

$$\begin{aligned} 2\boldsymbol{\epsilon}^n &= \mathbf{E}^n - \tilde{\mathbf{E}} + c^2\nabla\times\tilde{\mathbf{B}} - f_n H^2 * \tilde{\mathbf{J}} \\ &= \mathbf{E}^n - \bar{\mathbf{E}}^{n-1} + \frac{c^2}{2}\nabla\times\left(\bar{\mathbf{B}}^{n-1/2} + \mathbf{B}^{n+1/2} - \nabla\times\bar{\mathbf{E}}^{n-1}\right) - f_n H^2 * \tilde{\mathbf{J}}. \end{aligned} \tag{2.20}$$

A correction to $\mathbf{E}'^{n+1}$ is sought so that repushing the particles with $\mathbf{E}'^{n+1} = \tilde{\mathbf{E}} + 2\delta\mathbf{E}^n$ (note that this definition gives $\mathbf{E}'^n = \bar{\mathbf{E}}^{n-1} + \delta\mathbf{E}^n$) will reduce $\boldsymbol{\epsilon}^n$ to zero. Retention of only the first order (linear) terms in $\delta\mathbf{E}^n$ leads to the linear field corrector equation

$$\mathcal{L}\delta\mathbf{E}^n = \delta\mathbf{E}^n + \frac{c^2}{2}\nabla\times\nabla\delta\mathbf{E}^n + \frac{f_n}{2}H^2 * \frac{\delta\mathbf{J}}{\delta\mathbf{E}}\cdot\delta\mathbf{E}^n = \boldsymbol{\epsilon}^n, \tag{2.21}$$

where the last term on the left symbolically represents the plasma susceptibility. Equation 2.21 is solved for the adjustment $\delta\mathbf{E}^n$ and all of Eqs. 2.19 (except 2.19f) are advanced to the next time step.

The estimate of $\delta\mathbf{J}$ and solution of the resulting field corrector equation is taken up next. First, the expression of the plasma susceptibility indicated in Eq. (2.21) is made precise. Then a method for the iterative solution of the resulting variable-coefficient, linear, elliptic, vector equation is developed.

The plasma susceptibility is expressed in terms of the perturbation of the particle orbits caused by a change in the time-filtered electric field, $\delta\mathbf{E}^n$. Apparently from Eqs. (2.19a) and (2.19b), the change in the time-advanced particle data is given by

$$\delta\mathbf{x}_j = \delta\mathbf{v}_j$$
$$\left[\overleftrightarrow{1} + \frac{1}{2}(1+\gamma_\alpha)\mathbf{\Omega}_\alpha^n(\mathbf{x}_j^n) \times \overleftrightarrow{1}\right] \cdot \delta\mathbf{v}_j = \frac{q_\alpha}{q_e}\frac{m_e}{m_\alpha}\delta\mathbf{E}^n(\mathbf{x}_j^n),$$

or

$$\delta\mathbf{x}_j = \delta\mathbf{v}_j = \pm\frac{m_e}{m_\alpha}\overleftrightarrow{T}_\alpha \cdot \delta\mathbf{E}^n, \tag{2.22}$$

where the upper (lower) sign, as before, is for electrons (ions). The single particle susceptibility tensors of Eq. (2.22) are given by

$$\overleftrightarrow{T}_\alpha = (1+W_\alpha^2)^{-1}\left[\overleftrightarrow{1} - \mathbf{W}_\alpha \times \overleftrightarrow{1} + \mathbf{W}_\alpha\mathbf{W}_\alpha\right], \tag{2.23}$$

with

$$\mathbf{W}_\alpha = \frac{1}{2}(1+\gamma_\alpha)\mathbf{\Omega}_\alpha^n(\mathbf{x}_j^n).$$

Combination of Eqs. (2.22) and (2.19c) gives the susceptibility

$$\delta\mathbf{J}(\mathbf{m}) = \frac{1}{2}\sum_j \left[i(\mathbf{m}-\mathbf{x}_j^n) + i(\mathbf{m}-\tilde{\mathbf{x}}_j)\right]\overleftrightarrow{T}_\alpha \cdot \delta\mathbf{E}^n(\mathbf{x}_j^n) + \mathcal{O}(kv\Delta t). \tag{2.24}$$

The terms omitted from Eq. (2.24) are smaller than those written by the order of $kv\Delta t$, where k is the wave vector. Langdon[16] has included the next term in Eq. (2.24). In the sequel, such terms are consistently neglected. Thus, the formulation given here is stable and accurate for $kv\Delta t \lesssim 1$ as previously discussed for the electrostatic case.[11]

Proceeding as in Ref. 11 (and again neglecting terms of order $kv\Delta t$) the plasma response term in Eq. (2.23) may be approximated by simplifying the expression given in Eq. (2.24). The resulting field corrector equation is

$$\mathcal{L}\delta\mathbf{E}^n = \delta\mathbf{E}^n + \frac{c^2}{2}\nabla\times\nabla\times\delta\mathbf{E}^n + \frac{f_n}{2}H^2 * \overleftrightarrow{\chi}\cdot\delta\mathbf{E}^n = \epsilon^n, \tag{2.25}$$

where the susceptibility $\overleftrightarrow{\chi}$ is given by

$$\overleftrightarrow{\chi} = \sum_\alpha \left(\frac{m_e}{m_\alpha}\right)\bar{n}_\alpha \overleftrightarrow{T}_\alpha, \tag{I2.5}$$

and $\bar{n}_\alpha$ is the point particle number density of species α,

$$\bar{n}_\alpha(m) = \frac{1}{2}\sum_{j\epsilon\alpha}\left[i(\mathbf{m}-\mathbf{x}_j^n) + i(\mathbf{m}-\tilde{\mathbf{x}}_j)\right]. \tag{2.26}$$

As Langdon has pointed out,[16] taking the divergence of Eq. (2.25) reproduces exactly the scalar field corrector of Ref. 11.

The field corrector given by Eq. (2.25) is a variable-coefficient, elliptic equation for $\delta\mathbf{E}^n$. Global iterative methods have been used effectively for similar scalar equations previously.[11] The scalar field corrector for the electrostatic plasma was treated effectively by approximating the plasma response by that of a constant density plasma; then inverting this approximate inverse by Fourier transforms. A similar scheme was implemented for the vector corrector, Eq. (2.25). Convergence was found to be unreliable under rather moderate conditions. Two problems were observed. First, the assumption of constant density omits any information about density gradients which may be convected by $\delta\mathbf{E}^n$. If both species are strongly magnetized ($\Omega_e \gg \Omega_i \gg 1$), a convective charge separation arises from the ion polarization motion in a nonuniform plasma, even if charge neutrality holds. In the case when only the electron species is strongly magnetized ($\Omega_e \gg \Omega_i \lesssim 1$), this effect becomes even more pronounced. In that case, the electric drift of the electrons produces convection perpendicular to $\delta\mathbf{E}^n$, and the unmagnetized motion of the ions, convection parallel to $\delta\mathbf{E}^n$. Neglect of these convective terms makes the convergence of an iteration based on a constant density approximation quite unreliable. An attempt was made to improve the approximate inverse by including the coupling of nearest neighboring harmonics in the direction of

expected inhomogeneity. This leads to a cumbersome approximate inversion in which a complex, block-tridiagonal (with 3×3 blocks) system must be inverted. Convergence is improved but still unsatisfactory for such a scheme. A second difficulty observed suggests an improved iterative technique. The operator of Eq. (2.25) is very anisotropic in both $\mathbf{m}$ and $\mathbf{k}$ space. This anisotropy arises from the variation of the plasma response in the direction parallel and perpendicular to the magnetic field, $\mathbf{B}$, and from the separation of the transverse and longitudinal responses of the vacuum described by Maxwell's equations.

The separation of these various responses may be used advantageously in developing an iterative method for inverting Eq. (2.25). First, note that the operator of Eq. (2.25) may be written as the sum of two operators, $\mathcal{L} = \mathcal{L}_1 + \mathcal{L}_2$, where

$$\mathcal{L}_1 = 1 + \frac{c^2}{2}\nabla \times \nabla, \tag{I2.7}$$

and

$$\mathcal{L}_2 = \frac{f_n}{2} H^2 * \overleftrightarrow{\chi}. \tag{I2.8}$$

For the geometry considered here, either of these operators may be inverted independently with little effort by the use of Fourier transforms. For more complicated geometries, a combination of Fourier transformation for periodic coordinates and finite differences for a non-periodic coordinate may be used.[14]

A strategy for iteration of the field corrector may now be developed. Because of the anisotropy mentioned earlier, one of the operators $\mathcal{L}_i$ will be strongly dominant on part of the solution. An approximate adjustment is given by inverting each of the $\mathcal{L}_i$'s on that part of the error where $\mathcal{L}_i$ dominates and selecting the significant portion of the approximate solution obtained.

If the magnitude of each operator is estimated parallel and perpendicular to $\mathbf{B}$ and longitudinal and transverse to $\mathbf{k}$, this selection is easily accomplished. There are crossover regions where both operators are comparable. It is easy to see that in these regions, one half of the average of the two inverses will provide a good approximation to the solution.

The estimates for the magnitudes of $\mathcal{L}_i$ on the various part of the solution are now given. It is supposed that all vectors are divided into parts parallel and perpendicular to $\mathbf{B}$ and longitudinal and transverse to $\mathbf{k}$. Thus, writing $\mathcal{F}$ for Fourier analysis (transformation

from $\mathbf{m}$ to $\mathbf{k}$ space), the error $\boldsymbol{\epsilon}^n$ is decomposed as

$$\varepsilon^n_{\|L} = \mathcal{P}_{\|L}\varepsilon^n = \mathcal{F}^{-1}\frac{\mathbf{kk}}{k^2}\cdot\mathcal{F}\frac{\mathbf{BB}}{B^2}\cdot\boldsymbol{\epsilon}^n, \tag{2.30a}$$

$$\varepsilon^n_{\|T} = \mathcal{P}_{\|T}\varepsilon^n = \mathcal{F}^{-1}\left[\overleftrightarrow{1} - \frac{\mathbf{kk}}{k^2}\right]\cdot\mathcal{F}\frac{\mathbf{BB}}{B^2}\cdot\boldsymbol{\epsilon}^n, \tag{2.30b}$$

$$\varepsilon^n_{\perp L} = \mathcal{P}_{\perp L}\varepsilon^n = \mathcal{F}^{-1}\frac{\mathbf{kk}}{k^2}\cdot\mathcal{F}\left[\overleftrightarrow{1} - \frac{\mathbf{BB}}{B^2}\right]\cdot\boldsymbol{\epsilon}^n, \tag{2.30c}$$

and

$$\varepsilon^n_{\perp T} = \mathcal{P}_{\perp T}\varepsilon^n = \mathcal{F}^{-1}\left[\overleftrightarrow{1} - \frac{\mathbf{kk}}{k^2}\right]\cdot\mathcal{F}\left[\overleftrightarrow{1} - \frac{\mathbf{BB}}{B^2}\right]\cdot\boldsymbol{\epsilon}^n. \tag{2.30d}$$

The solution $\delta\mathbf{E}^n$ is similarly decomposed.

Only the diagonal parts of $\mathcal{L}_i$ are retained in the iteration. That is, after inverting $\mathcal{L}_i$ on, say, $\boldsymbol{\epsilon}^n_{\|L}$, only the $\|, L$ portion of the solution is retained. Thus, an estimate is required for the eight projections $\mathcal{L}_{i\|L}$, $\mathcal{L}_{i\|T}$, $\mathcal{L}_{i\perp L}$, $\mathcal{L}_{i\perp T}$. These are estimated as

$$\mathcal{L}_{1\|L} \sim 1, \tag{2.31a}$$

$$\mathcal{L}_{1\|T} \sim 1 + \frac{k^2c^2}{2}, \tag{2.31b}$$

$$\mathcal{L}_{1\perp L} \sim 1, \tag{2.31c}$$

$$\mathcal{L}_{1\perp L} \sim 1 + \frac{k^2c^2}{2}, \tag{2.31d}$$

$$\mathcal{L}_{2\|L} \sim \frac{f_n h^2 \bar{\rho}}{2}, \tag{2.31e}$$

$$\mathcal{L}_{2\|T} \sim \frac{f_n h^2 \bar{\rho}}{2}, \tag{2.31f}$$

$$\mathcal{L}_{2\perp L} \sim \frac{f_n h^2 \bar{\rho}}{2\left[1 + \left(\frac{1}{2} + \gamma\right)\bar{\Omega}_e\right]}, \tag{2.31g}$$

and

$$\mathcal{L}_{2\perp T} \sim \frac{f_n h^2 \bar{\rho}}{2\left[1 + \left(\frac{1}{2} + \gamma\right)\bar{\Omega}_e\right]}, \tag{2.31h}$$

where $\bar{\rho}$, $\bar{\Omega}_e$ are mean values for ρ and Ω_e. Using these estimates for the eight projections, an approximate inverse to $\mathcal{L}$ may be written as

$$\mathcal{L}^{-1} \sim \mathcal{M} = \mathcal{P}_{\|L}\left[\left(\frac{\mathcal{L}_{1\|L}}{\mathcal{L}_{1\|L} + \mathcal{L}_{2\|L}}\right)^2 \mathcal{L}_1^{-1} + \left(\frac{\mathcal{L}_{2\|L}}{\mathcal{L}_{1\|L} + \mathcal{L}_{2\|L}}\right)^2 \mathcal{L}_2^{-1}\right]\mathcal{P}_{\|L} + \{\|T\} + \{\perp L\} + \{\perp T\} \tag{2.32}$$

where the terms shown schematically are the same as the first with the appropriate subscripts substituted.

This approximate inverse $\mathcal{M}$ is then used to construct an iterative scheme for the solution of Eq. (2.25),

$$^{l+1}\delta\mathbf{E}^n - ^{l}\delta\mathbf{E} = \mathcal{M}\left\{\varepsilon^n - \mathcal{L}^l\delta\mathbf{E}^n\right\} \tag{2.33}$$

where l labels the iteration level.

III. Code Tests

In this section, test results obtained from a one-dimensional code based on the low-frequency electromagnetic algorithm of Sec. II are presented. The second-order accurate implicit scheme described there is used with area weighting interpolation of the charge density and currents from, and of the forces to, the particles. The wave dispersion and fluctuation properties of a uniform, thermal, magnetized, two-temperature plasma are examined.

The test parameters are (system length) $N_x = 256\Delta$, (number of particles) $N_0 = 10240$, (particle size) $a = 1.5\Delta$, where Δ is the grid spacing with Gaussian particle shape represented by $h = \exp(-k^2a^2/2)$, (ion-to-electron mass ratio) $m_i/m_e = 100$, (electron-to-ion temperature ratio) $T_e/T_i = 20$. The constant magnetic field lies in the x-z plane at an angle ϕ from the x-axis which is the wavevector direction. It is of strength such that $\Omega_e/\omega_e = 1.0$. The speed of light c is set at $c/\omega_e\Delta = 1.0$ and the Alfvén velocity scales as $v_A/c = \Omega_i/\omega_i = 0.1$. Electrons and ions are initially loaded uniformly on the one-dimensional spatial grid with zero perpendicular thermal velocity. The time centering parameters are such that $\gamma_e = \gamma_i = 0.1$ and both electrons and ions are treated implicitly.

Stability and accuracy dictate that $kv\Delta t < 1$ with v the maximum of the trapping velocity and the average fluid velocity, each closely related to the thermal velocity v_T, and $v_T \cos\phi\Delta t/\Delta < 1$. This suggests two ways to achieve large time steps; either decrease the thermal velocity, i.e., decrease v, or increase the grid spacing Δ with respect to the unit grid spacing δ by a stretch factor Δ/δ, i.e., decrease k. The latter is adopted here.

The parallel electron and ion distribution functions are taken to be Maxwellian. The thermal velocity of the electrons is chosen such that $v_{Te}/\omega_e\Delta = 5 \times 10^{-2}$, so that the electron Debye length is $\lambda_{De}/\Delta = 5 \times 10^{-2}$. The time-step can then be chosen as $\omega_e\Delta t = 10$, 10^2, 10^3 with grid spacing $\Delta = \delta$, 10δ, 100δ. This represents a factor of 10^2 to 10^4 increase over that allowed for an explicit code in which ω_e has to be resolved. The calculation comprises 8,192 time steps so that many ion-acoustic and Alfvén wave periods are resolved. Since the plasma is nearly uniform, the iterative solution of the implicit field equation requires only two iterations to converge to a relative error of 10^{-5} of the equivalent mean density. No iteration of the particle pushing beyond the first correction

has ever been necessary.

The collective behavior of the plasma at frequencies $\omega \ll \omega_e$ is displayed in Figs. 1-4 for wave propagation parallel, oblique and perpendicular to the magnetic field.

For purely parallel propagation ($\phi = 0$), the electrostatic and electromagnetic low frequency modes predicted by a theoretical analysis are the ion-acoustic waves, the Whistler waves and the shear Alfvén waves. For one set of parameters, the simulation plasma can only carry waves within a range of wavelengths delimited by the system length and spatial grid size or particle size. Since we use two independent values of Δ or two sets of values of k, but with the same ratio $\lambda_D/\Delta = 0.05$, all of the results from these two runs are combined into one figure over a range of three decades of $k\lambda_D$. The measured frequencies thus obtained are shown by triangles ($\Delta/\delta = 10$) and circles ($\Delta/\delta = 1$) in Figs. 1a and b. The frequency, ω/ω_e, varies over a four decade range. No mode frequencies higher than the ones plotted were observed in the spectrum. Comparison with theoretical predictions is carried out as follows. The electromagnetic modes can be extracted from the cold plasma dispersion relation

$$\tan^2\phi = -\frac{\left(\frac{1}{n^2}-\frac{1}{\varepsilon_R}\right)\left(\frac{1}{n^2}-\frac{1}{\varepsilon_L}\right)}{\left(\frac{1}{n^2}-\frac{1}{\varepsilon}\right)\left(\frac{1}{n^2}-\frac{1}{2}\left(\frac{1}{\varepsilon_R}+\frac{1}{\varepsilon_R}\right)\right)}, \tag{3.1a}$$

$$n^2 = k^2c^2/\omega^2 \tag{3.1b},$$

$$\varepsilon_{R,L} = 1 - \frac{h^2\omega_e^2}{\omega(\omega \mp \Omega_e)} - \frac{h^2\omega_i^2}{\omega(\omega \pm \Omega_i)}, \tag{3.1c}$$

$$\varepsilon = 1 - (\omega_e^2 + \omega_i^2)h^2/\omega^2, \tag{3.1d}$$

where h^2 is the particle shape factor. The ion-coustic dispersion relation for $\omega \ll \Omega_i$ is obtained from[11]

$$\varepsilon = 1 + \frac{h^2}{k^2\lambda_{De}^2}\left(1 + \frac{\omega}{\sqrt{2}k_\parallel v_{Te}} Z\left(\frac{\omega}{\sqrt{2}k_\parallel v_{Te}}\right)\right) + \frac{h^2}{k^2\lambda_{Di}^2}\left(1 + \frac{\omega}{\sqrt{2}k_\parallel v_{Ti}} Z\left(\frac{\omega}{\sqrt{2}k_\parallel v_{Ti}}\right)\right), \tag{3.2}$$

with $k_{||} = k\cos\phi$. An approximate solution to Eq. (3.2) gives $\omega/\omega_e \simeq (m_e/m_i)^{1/2}k_{||}\lambda_{De}\left[(1+3T_i/T_e)/(1+k^2\lambda_{De}^2h^{-2})\right]^{1/2}$. The dispersion relations ω/ω_e versus $k\lambda_D$ obtained from numerical solutions of these equations with $\phi = 0$ are shown as solid curves in Figs. 1a and b. Excellent agreement is clear with the low frequency branches, the first curve from the bottom being the ion-acoustic one, the second the shear Alfvén or Alfvén ion cyclotron one and the third the whistler branch.

The time averaged electrostatic energy per wave number $\left\langle E_{Lk}^2/8\pi\right\rangle$ normalized to the thermal energy per degree of freedom $\kappa_B T_e/2$ (with κ_B Boltzmann's constant), or fluctuation spectrum, is shown in Fig. 2 for the same two runs with $\phi = 0$. For $T_e \gg T_i$ and $\omega \ll \omega_e$, Ω_e, the fluctuation spectrum of a two temperature Maxwellian plasma can be written as[11]

$$\frac{\left\langle E_{Lk}^2/8\pi\right\rangle}{\kappa_B T_e/2} \sim \frac{k^2\lambda_{De}^2h^2}{1+k^2\lambda_{De}^2h^2}. \tag{3.3}$$

The fluctuation spectrum predicted by Eq. (3.3) is plotted as the upper curve in Fig. 2. The fluctuation spectrum measured in the simulations indicated by triangles ($\Delta/\delta = 10$) and circles ($\Delta/\delta = 1$) follows closely the prediction of Eq. (3.3). The lower curve is the spectrum one would obtain with Boltzman electrons, i.e., in the absence of electron Landau damping.[11]

As the angle ϕ between the wavenumber (or x-axis) and the magnetic field is increased from 0° to 90°, the Whistler wave merges with the compressional Alfvén wave. The shear Alfvén wave frequency goes to zero in the limit of purely perpendicular propagation. For $0 < \phi < 90°$, the three branches coexist. Results for propagation with $\phi = 45°$ are displayed in Fig. 3. The simulation frequencies, measured in the three components of the electric field E_x (Fig. 3a), E_y (Fig. 3b) and E_z (Fig. 3c) are plotted as circles. Only one value for the grid spacing, Δ, $\Delta/\delta = 1$, is used so that the wavevector varies over two decades and the frequency over four. There is excellent agreement between simulation and the theoretical dispersion relations of Eqs. (3.1) and (3.2) represented by curves in Fig. 3, the first from the bottom being the ion-acoustic branch, the second the Alfvén or Alfvén Ion Cyclotron branch and the third the whistler cum magnetosonic branch.

For purely perpendicular propagation, only the compressional Alfvén or magnetosonic wave is predicted as a low frequency mode. The dispersion relation for perpen-

dicular propagation ($\phi = 90°$) is presented in Fig. 4. Three values of the stretch factor, $\Delta/\delta = 1$, 10 and 100, are used in the simulations and the results from these three runs again combined into one diagram. The wavevector varies over four decades, the frequencies represented by plusses ($\Delta/\delta = 100$), triangles ($\Delta/\delta = 10$) and circles ($\Delta/\delta = 1$). Agreement with the lower curve obtained from cold plasma theory including finite particle size effects (Eq. 3.1) for the compressional Alfvén wave is excellent.

The following observations are suggested by the results shown in Figs. 1-4. As the time step Δt is raised (as is possible here when Δ is increased or v_T is lowered), the observable frequency range, $\omega_{\min} < \omega < \omega_{\max}$, shifts toward smaller ω in accordance with $\omega_{\max}\Delta t < 1$ and $\omega_{\min} = \omega_{\max}/N_t$, with N_t the total number of time steps in a run. This is the natural frequency filtering intrinsic to the algorithm of Sec. II. Raising the time step Δt also has the consequence that the resolvable wave vector range $k_{\min} < k < k_{\max}$ shifts toward smaller k. The maximum wavevector is set by $k_{\max}v\Delta t < 1$ and for waves such that $\omega = kv_{ph}$, (as is the case here with v_{ph} the phase velocity of the wave), also by $k_{\max}v_{ph}\Delta t < 1$ since $\omega_{\max}$ $(= k_{\max}v_{ph})$ $\Delta t < 1$. The minimum resolvable wavenumber $k_{\min}$ is set either by the limit of the spatial resolution $k_{\min} = 2\pi/N_x\Delta$ or by the limit of the temporal resolution $k_{\min} = \omega_{\min}/v_{ph}$ for waves such that $\omega = kv_{ph}$, whichever is larger. Therefore increasing Δt within the constraints of stability and accuracy provides a natural zoom towards both the longer time scales and the larger space scales. We note that raising Δt by lowering v_T has the consequence that the wavevector k of the scope of the simulation becomes small with respect to k_{De} $(= \lambda_{De}^{-1}) = \omega_e/v_T$ since $k_{De} \to \infty$ as $v_T \to 0$. Raising Δt by increasing Δ makes $k = 2\pi m/N_x\Delta$ small with respect to k_{De} simply because Δ is larger. In our implicit code, both making v_T smaller or Δ larger, therefore focusing on ranges of smaller frequencies or longer wavelengths, are possible without causing numerical instability. Little flexibility exists to do so in explicit codes.

The one-dimensional test results of this section clearly demonstrate the accuracy of the implicit method of Sec. II for studying low frequency phenomena in a thermal plasma. The dispersion relations and fluctuation spectra measured in the simulations agree very well with theoretical expectations. The results of this section also show the implicit algorithm makes it possible to increase the simulated spatial scale with respect to the Debye length

or collisionless skin depth and therefore possible to focus on phenomena of any range of frequency and wavelength.

IV. Applications

Applications of an electromagnetic code, based on the direct implicit algorithm of Sec. II, to two instabilities of a magnetized two-and-one-half-dimensional plasma are now presented. The first is a simulation of the collisionless tearing instability for a plasma carrying a current along the magnetic field. It is set up so as to be directly comparable to a previous explicit simulation of the same instability by Katanuma and Kamimura.[17] The second is a simulation of the closely related coalescence instability of two such current filaments.

IV.1 Collisionless Tearing Instability

The collisionless tearing simulation is carried out in a configuration with (system size) $N_x \times N_y = 64 \times 32$ with $\Delta_y/\delta = 2$, (number of electrons or ions) $N_0 = 18,432$, (mass ratio) $m_i/m_e = 16$, (electron cyclotron frequency) $\Omega_e = 1.5\omega_e$, (speed of light) $c/(T_e/m_e)^{1/2} = 10$ and (particle size) $a = 1.5$. The uniform external magnetic field B_z is normal to the plane of the simulation. A shear magnetic field $B_y(x)$ is produced by a sheet current along B_z. The perturbed vector potential $\tilde{A}_z$ obeys the following equation[17]

$$\left(\frac{\partial^2}{\partial x^2} - k_y^2\right)\tilde{A}_z = \frac{1}{c^2\lambda_{De}^2}\left\{\omega\left[\left\langle\left\langle v_\parallel^2\right\rangle\right\rangle - v_{0z}\left\langle\langle v_\parallel\rangle\right\rangle\right]\right.$$
$$\left. - k_y/\Omega_e\left[\left\langle\left\langle v_\parallel^3\right\rangle\right\rangle - v_{0z}\left\langle\left\langle v_\parallel^2\right\rangle\right\rangle\right]\frac{\partial}{\partial x}v_{0z}\right\|\right\}\tilde{A}_z, \tag{4.1}$$

where $\left\langle\left\langle v_\parallel^n\right\rangle\right\rangle = \int dv \frac{v_\parallel^n}{\omega - k_\parallel v_\parallel} f_0(v)$, with the initial current profile being

$$J_z(x) = -J_{0z}\exp\left[-(\ell n 2)(x - L_x/2)^2/a_0^2\right], \tag{4.2}$$

with $a_0 = 5.1\Delta$ the initial width of the current channel and $J_{0z} = en_0(T_e/m_e)^{1/2}$. The electrons and ions are initially loaded with their guiding center velocities $\mathbf{v}_\perp = 0$ in such a way that the initial density of the particles with uniform parallel temperature balances the shear magnetic field pressure $B_y^2(x)/8\pi$. The system is bounded in x by conducting walls and periodic in y.

The explicit simulations of Katanuma and Kamimura[17] used a full dynamics magneto-inductive particle model and the time step $\Delta t = 0.1\omega_e^{-1}$. The time step used

in the present implicit simulation is $\Delta t = 10\omega_e^{-1}$ or a two order of magnitude increase over the explicit code. To optimize code performance in achieving such a large time step, a decentering parameter value of $\gamma_e = \gamma_i = 0.1$ is used in the implicit simulations. This means that both electrons and ions are treated implicitly.

The collisionless tearing simulation results are summarized in Figs. 5,6 and 7. The plasma is initially perturbed by a mode with the longest wavelength in y, $k_y = 2\pi/N_y\Delta_y$, which is the only unstable mode according to the linear analysis.[18] Figures 5 and 6 show various snapshots of magnetic flux and magnetic field B_x doubled periodically in the y-direction for presentation. As can be seen from Figs. 5 and 6, the formation and growth of a magnetic island near the middle of the simulation domain evolves in a manner very much similar to what has been observed in the explicit simulation of Katanuma and Kamimura.[17] As in their work, the tearing instability goes through the linear growth stage,[18] the nonlinear growth or Rutherford stage [19,20] and the nonlinear saturation stage, the time evolution of the magnetic island width W normalized to its maximum value of $2.1a_0$ is shown in Fig. 7. In the nonlinear growth stage, the measured island width is approximately proportional to time, which is characteristic of the Rutherford phase.[19,20] The physical mechanism of saturation is provided by the flattening of the current.

Analysis of the results is complicated by the fact that, in contrast to the usual theoretical assumption of a given constant Δ', the simulations solve an initial value problem where the initial electron current and its initial profile are evolved. The linear growth rate of the tearing instability is expressed as [18]

$$\gamma_L = k_y v_e \Delta' / 2\pi^{1/2} (\omega_e/c)^2 L_s, \tag{4.3}$$

where L_s is the shear strength and

$$\Delta' = \left[\frac{\partial}{\partial x} \tilde{A}_z \left(L_x/2 + \lambda \right) - \frac{\partial}{\partial x} \tilde{A}_z \left(L_x/2 - \lambda \right) \right] / \tilde{A}_z \left(L_x/2 \right). \tag{4.4}$$

Here λ stands for the singular layer width determined by the electron Doppler shift condition along the magnetic field lines $k_{\|} \left(x = L_x/2 + \lambda \right) \times v_e = \gamma_L$ and λ therefore depends on Δ'. It is not easy to assign a value to Δ' here since the profile of the perturbed current channel ("singular layer") is less abrupt in the simulations than is assumed in theory and

is also strongly time dependent. Nevertheless, Eq. (4.3) with $L_s \simeq 170\Delta$, $\Delta' \simeq a_0^{-1}$, and $k_y \simeq 0.1$ yields $\gamma_L \simeq 3 \times 10^{-3}\omega_e$, while the measured growth rate is $\gamma \sim 10^{-3}\omega_e$. The simulation value is however in close agreement with a shooting code solution of Eq. (4.1) which yields $\gamma_L \simeq 1.3 \times 10^{-3}\omega_e$.

The Rutherford nonlinear growth stage quickly follows the linear growth stage. According to Drake and Lee,[19] the island width W in this stage grows as

$$W = \frac{1}{16G}\left(\frac{c}{\omega_e}\right)^2 \Delta' \nu t, \tag{4.5}$$

where $G \simeq 0.41$ and ν is the collision frequency. If we take $\Delta' \sim a_0^{-1}$, which is clearly a crude estimate of Δ', and if we use the effective collision frequency due to finite size particles,[2] $\nu \simeq 1.4 \times 10^{-3}\omega_e$, we get $W/a_0 \sim 0.82 \times 10^{-3}\omega_e t$ for the parameters of the simulation. This theoretical estimate is only in qualitative agreement with the simulation results of Fig. 7 because of the ambiguity in the definition of Δ'.

IV.2. Coalescence Instability

The second application is to the coalescence instability driven by the attractive force between current filaments. Pritchett and Wu[21] investigated the coalescence instability with an MHD code. This instability evolves on an essentially MHD time scale in the linear stage.

Our implicit particle simulations are carried out with the following parameters (system size) $N_x \times N_y = 32 \times 64$, (number of electrons or ions) $N_0 = 18,432$, (mass ratio) $m_i/m_e = 16$, (Debye length) $\lambda_{De} = 1\Delta$, (electron cyclotron frequency) $\Omega_e = 1.5\omega_e$, (temperature ratio) $T_e/T_i = 1$, (speed of light) $c/\omega_e\Delta = 10$, (time step) $\Delta t = 5\omega_e^{-1}$. The system is bounded in x and periodic in y. Also, the decentering parameters are chosen such that $\gamma_e = 0.1$ and $\gamma_i = 0$ so that the electrons are implicit but the ions are treated explicitly ($\Omega_i \Delta t < 1$).

The initial magnetic field configuration is chosen as[22]

$$B_x = B_{0y}\frac{\varepsilon \sin ky}{\cosh kx + \varepsilon \cos ky}, \tag{4.6a}$$

$$B_y = B_{0y}\frac{\sinh kx}{\cosh kx + \varepsilon \cos ky} \tag{4.6b}$$

$$B_z = \left[B_{0y}^2 \frac{1-\varepsilon^2}{(\cosh kx + \varepsilon \cos ky)^2} + B_{0z}^2 \right]^{1/2} \tag{4.6c}$$

and $n(x) = \text{const.}$. Here typically $B_{0y}/B_{0z} = 0.0435$. The current peakedness parameter ε is varied from 0.05 to 0.85. The Alfvén transit time across half a magnetic island is approximately $\tau_h \simeq 30\omega_e^{-1}$.

Results of the simulations are displayed in Figs. 8 and 9. Figure 8a shows the time evolution of the amplitude of the magnetic field B_x with $\varepsilon = 0.3$ for two wavenumbers $k_y = 2\pi \times 1/N_y$ and $k_y = 2\pi \times 2/N_y$. The fundamental mode is unstable as expected.[21] The measured growth rate in this case is $\gamma_L \sim 6.2 \times 10^{-3}\omega_e$. The (approximately) corresponding case of Pritchett and Wu[21] is the one with their $x_w = 5$ (from the aspect ratio) and small S. In their calculation, however, the toroidal field given by Eq. (4.6c) does not contain B_{0z}. Their growth rate is $\gamma_{\text{MHD}} \approx 0.145\tau_h^{-1}$. With our estimate of $\tau_h \approx 30\omega_e^{-1}$, this gives $\gamma_{\text{MHD}} \sim 4.8 \times 10^{-3}\omega_e$, in order of magnitude agreement with our simulation.

Figure 8b shows the linear growth rate versus ε (the current peakedness parameter) measured in our simulations. Also shown is the Pritchett and Wu[21] growth rate for $x_w = 5$ evaluated with our τ_h. Both agree in the qualitative dependence on ε. Quantitative agreement can only be fair because of the different B_{0z}'s and plasma betas.

Figure 9 displays the measured linear growth rate of the coalescence mode ($k_y = 2\pi \times 1/N_y$) as a function of B_{0z}. It shows the interesting tendency of the linear growth rate to decrease with increasing B_{0z}, the z component of the toroidal field.

These results demonstrate good qualitative agreement and reasonable quantitative agreement between MHD theory and our implicit simulations of the coalescence instability.

The two applications presented in this section demonstrate the efficacy of the direct implicit electromagnetic algorithm described in Sec. II when applied to low frequency electromagnetic phenomena in strongly magnetized, inhomogeneous and bounded plasmas.

V. Discussion

We have presented a direct implicit electromagnetic algorithm for the particle simulation of low frequency phenomena in strongly magnetized plasmas. It is an involved extension of our direct implicit electrostatic algorithm.[11] It shares with it some of the keys to its success, such as simplified differencing to properly account for finite particle size effects in the implicit field solve and straightforward time decentering of the Lorentz force to allow time steps such that $\Omega_e \Delta t \gg 1$.

Our algorithm is close in spirit to the direct implicit electromagnetic algorithm of Langdon[16] and Hewett and Langdon.[12] The latter, however, appears to be applicable to weakly magnetized plasmas only since gyromotion is retained in the Lorentz force pushing the particles. We note that the implicit electromagnetic moment method[10] is also limited in this way. Some other important differences exist between our algorithm and that of Langdon[16] and Hewett and Langdon.[12] We introduce time filtering into Ampere's law rather than Faraday's law so that the magnetic field advance remains completely explicit. Also, we correct the electric field instead of the current to insure charge conservation. Finally, because of the strong coupling of the electric field components imposed by the implicit field solve, they advocate a simultaneous splitting solution of the field equations using matrix techniques. We elect to build an approximate inverse of the operators relating the desired fields to their sources in the implicit field solver, separating the plasma response into parts parallel and perpendicular to the magnetic field and into parts longitudinal and transverse to the wavevector. The field components are then obtained by a rapidly convergent iterative technique in Fourier space.

Our extensive code tests show that our direct implicit algorithm reproduces accurately the low frequency electrostatic and electromagnetic dispersion and fluctuation properties of a uniform plasma with time steps as large as $\omega_e \Delta t = 10^3$. The algorithm is naturally able to follow time scales much longer than the electron plasma or cyclotron period and space scales much larger than the Debye length or collisionless skin depth.

Our applications to the collisionless tearing instability and the coalescence instability demonstrate the efficacy of the algorithm in the following ways. The collisionless tearing instability has been evolved to saturation at a fraction of the cost of an explicit

magneto-inductive code run with equivalent parameters. The coalescence instability runs show that the algorithm is able to tackle MHD time scales but with kinetic low frequency effects properly accounted for.

Acknowledgments

We would like to acknowledge many useful discussions with Y. Abe, J.U. Brackbill, B.I. Cohen, D. Hewett, A.B. Langdon, Y. Ohara, and M.N. Rosenbluth. This work was supported by the U.S. Department of Energy, under contract no. DE-FG05-80ET-53088, the National Science Foundation grant NSF-ATM85-06646, and by the Ministry of Education of Japan under the U.S./Japan Joint Institute for Fusion Theory (JIFT).

References

1. K.V. Roberts and D.E. Potter, in *Methods in Computational Physics*, B. Alder et al., Eds., Vol. 9, p. 339, Academic Press, New York, 1970; J.U. Brackbill, in *Methods in Computational Physics*, B. Alder et al., Eds., Vol. 16, p. 1, Academic Press, New York, 1976.
2. J.M. Dawson in *Methods in Computational Physics*, B. Alder et al., Eds., Vol. 9, p. 1, Academic Press, New York, 1970; C.K. Birdsall, A.B. Langdon and H. Okuda, ibid, p. 241.
3. A.B. Langdon, J. Comp. Phys. **30**, 202 (1979).
4. R.J. Mason, J. Comp. Phys. **41**, 233 (1981).
5. J. Denavit, J. Comp. Phys. **42**, 337 (1981).
6. A. Friedman, A.B. Langdon and B.I. Cohen, Comm. Plas. Phys. Cont. Fusion **6**, 225 (1981).
7. B.I. Cohen, A.B. Langdon and A. Friedman, J. Comp. Phys. **46**, 15 (1982).
8. A.B. Langdon, B.I. Cohen and A. Friedman, J. Comp. Phys. **51**, 107 (1983).
9. A.B. Langdon and D.C. Barnes, in *Computational Techniques*, B. Alder and S. Fernbach, Eds., Vol. 3, p. 336, Academic Press, New York, 1985.
10. J.U. Brackbill and D.W. Forslund, J. Comp. Phys. **46**, 271 (1982); J.U. Brackbill and D.W. Forslund, in *Computational Techniques*, B. Alder and S. Fernbach, Eds., Vol. 3, p. 272, Academic Press, New York, 1985.
11. D.C. Barnes, T. Kamimura, J-N. Leboeuf, and T. Tajima, J. Comp. Phys. **52**, 480 (1983).
12. D.W. Hewett and A.B. Langdon, in *Laser Program Annual Report, 1984*, UCRL-80021-84, p. 2.4.8, Lawrence Livermore National Laboratory, Livermore, California, 1985.
13. T. Kamimura, T. Tajima, J-N. Leboeuf and D.C. Barnes, Bull. Am. Phys. Soc. **27**, 1035 (1982).
14. E. Montalvo, D.C. Barnes, T. Kamimura, J.N. Leboeuf and T. Tajima, Bull. Am. Phys. Soc. **30**, 1368 (1985).

15. A.B. Langdon and B.F. Lasinski, in *Methods in Computational Physics*, B. Alder et al., Eds., Vol. 16, p. 327, Academic Press, New York, 1976.
16. A.B. Langdon in *Laser Program Annual Report, 1982*, UCRL-80021-32, p. 3-53, Lawrence Livermore National Laboratory, Livermore, California, 1985.
17. I. Katanuma and T. Kamimura, Phys. Fluids **23**, 2500 (1980).
18. J. Drake and Y.C. Lee, Phys. Fluids **20**, 1341 (1977).
19. P. Rutherford, Phys. Fluids **16**, 1903 (1973).
20. J. Drake and Y.C. Lee, Phys. Rev. Lett. **39**, 653 (1977).
21. P. Pritchett and C.C. Wu, Phys. Fluids **22**, 2140 (1979).
22. V.M. Fadeev, I.F. Kvartskhava and N.N. Komarov, Nucl. Fusion **5**, 202 (1965).

Figure Captions

Fig. 1. One dimensional code tests for propagation parallel to the magnetic field. Dispersion relation, ω/ω_e vs. $k\lambda_D$, for a) the electrostatic branch and b) the electromagnetic one. Measured simulation frequencies are indicated by triangles for a stretch factor $\Delta/\delta = 10$ and circles for $\Delta/\delta = 1$. The theoretical dispersion relations are drawn in as curves, the first from the bottom being the ion-acoustic branch, the second the shear Alfvén one and the third the whistler branch. The abscissas and ordinates are labeled in powers of 10.

Fig. 2. One dimensional code tests for parallel propagation. Electrostatic fluctuation spectrum, $\left\langle E_{Lk}^2/8\pi \right\rangle / (\kappa_B T_e/2)$ vs. $k\lambda_D$. Simulation values are indicated by triangles and circles. The upper curve depicts the theoretical spectrum in the presence of electron Landau damping, the lower curve without.

Fig. 3. One dimensional code tests for propagation oblique to the magnetic field with angle $\phi = 45°$. Dispersion relation, ω/ω_e vs. $k\lambda_D$, measured in the three components of the electric field a) E_x, b) E_y and c) E_z. The simulation frequencies are plotted as circles and theoretical predictions as curves, the first from the bottom representing the ion acoustic branch, the second the shear Alfvén branch and the third, the whistler cum magnetosonic branch.

Fig. 4. One dimensional code tests for propagation perpendicular to the magnetic field. Dispersion relation ω/ω_e vs. $k\lambda_D$. Simulation frequencies are represented by plusses (stretch factor $\Delta/\delta = 100$), triangles ($\Delta/\delta = 10$), circles ($\Delta/\delta = 1$), while the lower curve is the theoretical dispersion relation for the magnetosonic mode.

Fig. 5. Two dimensional simulation of the collisionless tearing instability. Snapshots of magnetic flux contours at various times in the simulation.

Fig. 6. Two dimensional simulation of the collisionless tearing instability. Snapshots of contours of the x component of the magnetic field B_x at various times in the simulation.

Fig. 7. Two dimensional simulations of the collisionless tearing instability. Measured island width, W, as a function of time in the nonlinear growth and saturation phase.

Fig. 8. Two dimensional simulations of the coalescence instability. a) Time evolution of the amplitude of the magnetic field B_x with $\varepsilon = 0.3$ for two wave numbers

$k_y = 2\pi \times 1/N_y$ and $k_y = 2\pi \times 2/N_y$. b) Measured linear growth rate γ/ω_e versus current peakedness ϵ for the coalescence mode $k_y = 2\pi \times 1/N_y$.

Fig. 9. Two dimensional simulations of the coalescence instability. Measured linear growth rate of the coalescence mode $k_y = 2\pi \times 1/N_y$ as a function of toroidal magnetic field strength B_{0z}.

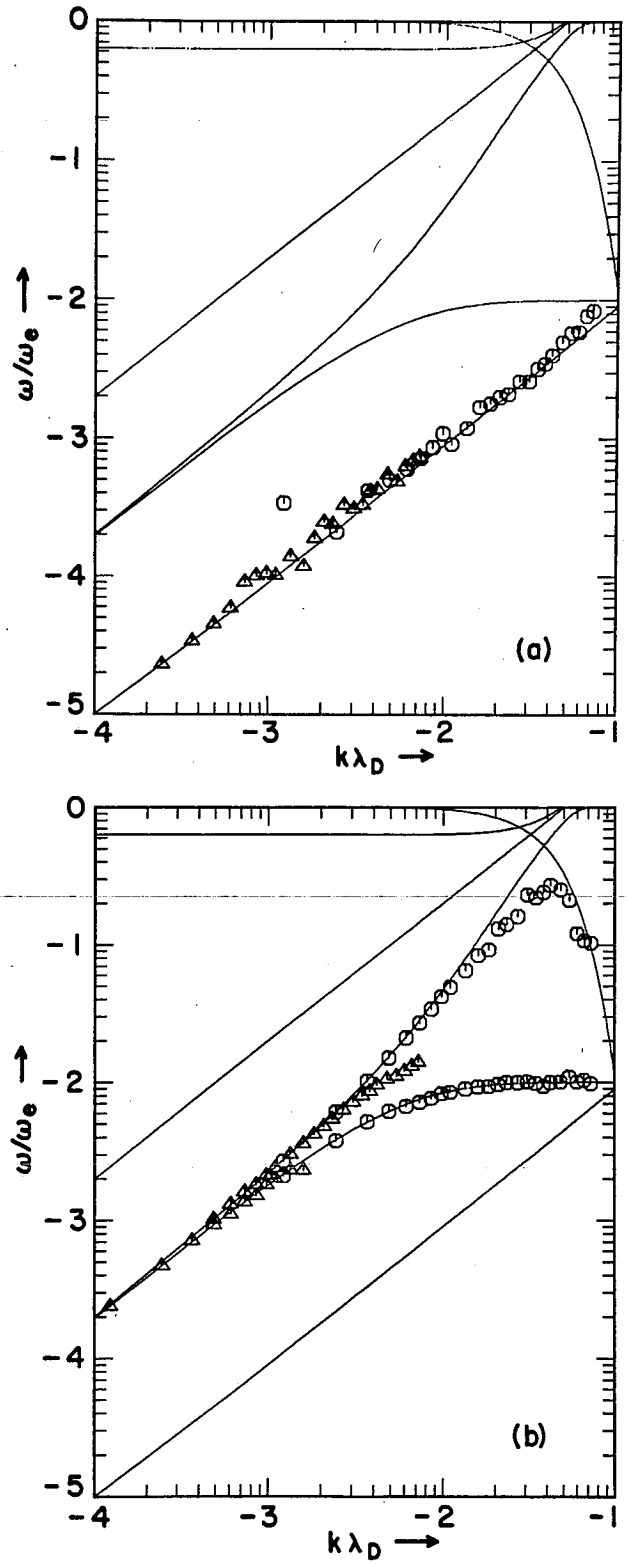

Figure 1

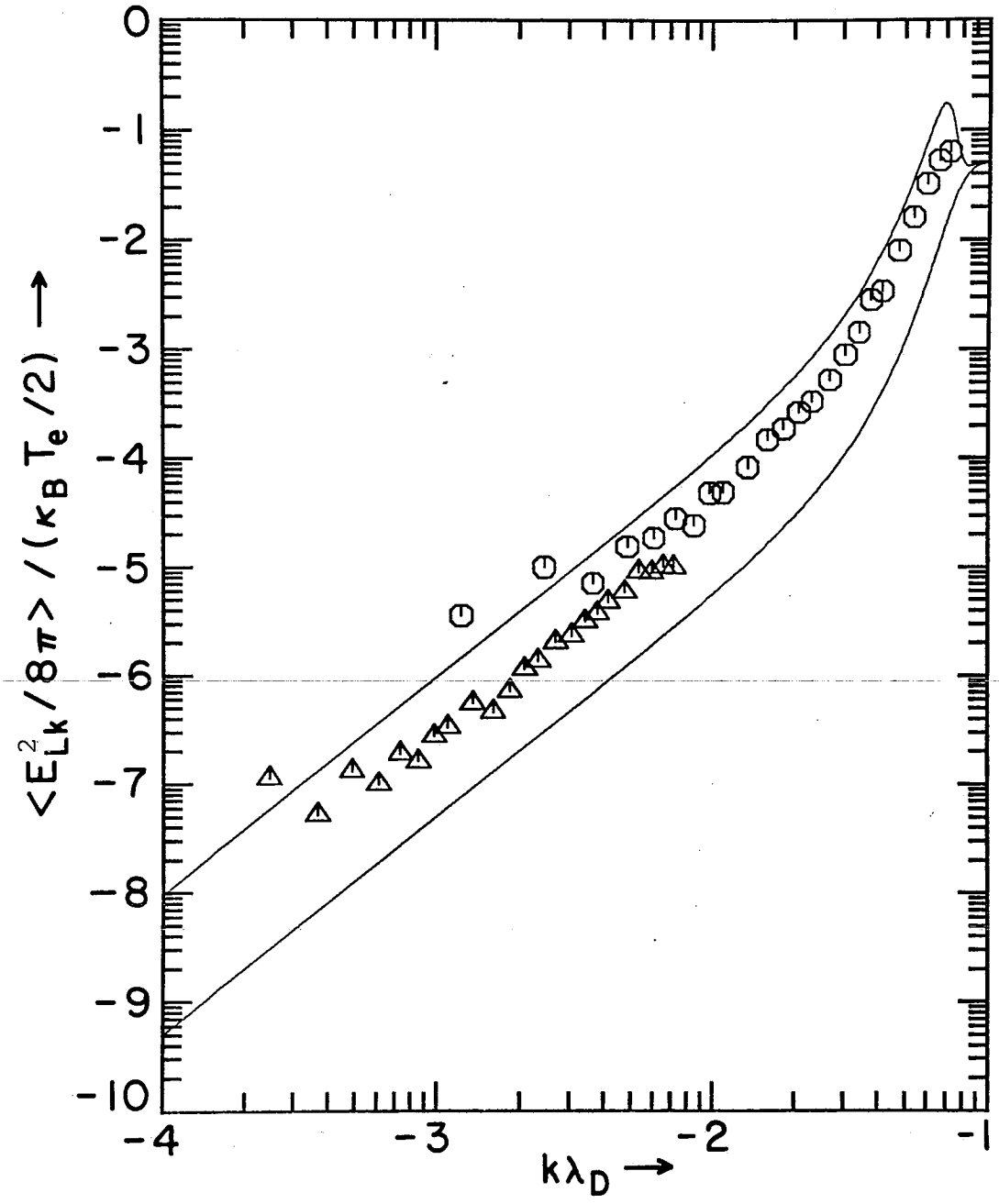
0
-1
-2
-3
-4
-5
-6
-7
-8
-9
-10
-4
-3
-2
-1
$\langle E_{Lk}^2/8\pi \rangle / (\kappa_B T_e/2) \longrightarrow$
$k\lambda_D \longrightarrow$

Figure 2

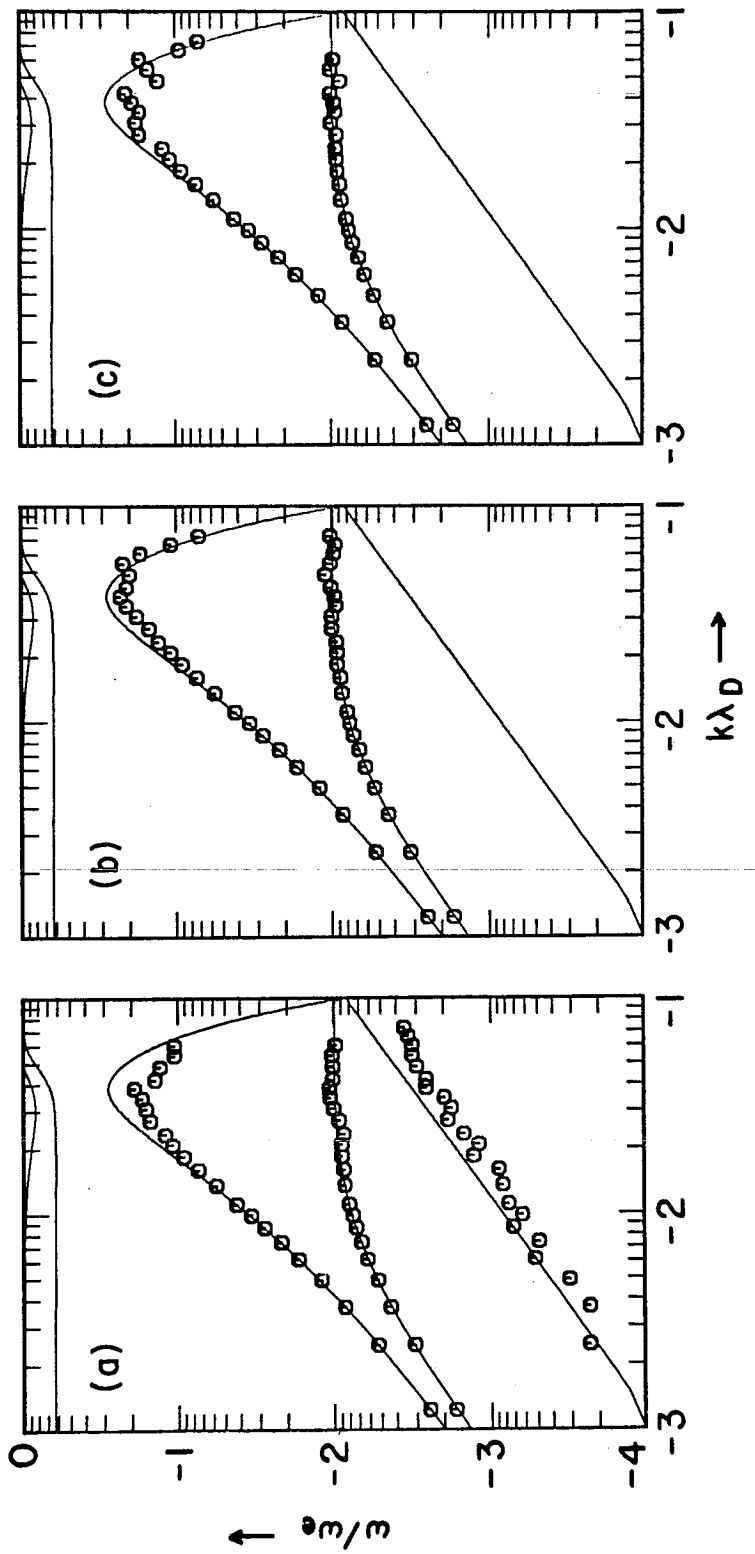

Figure 3

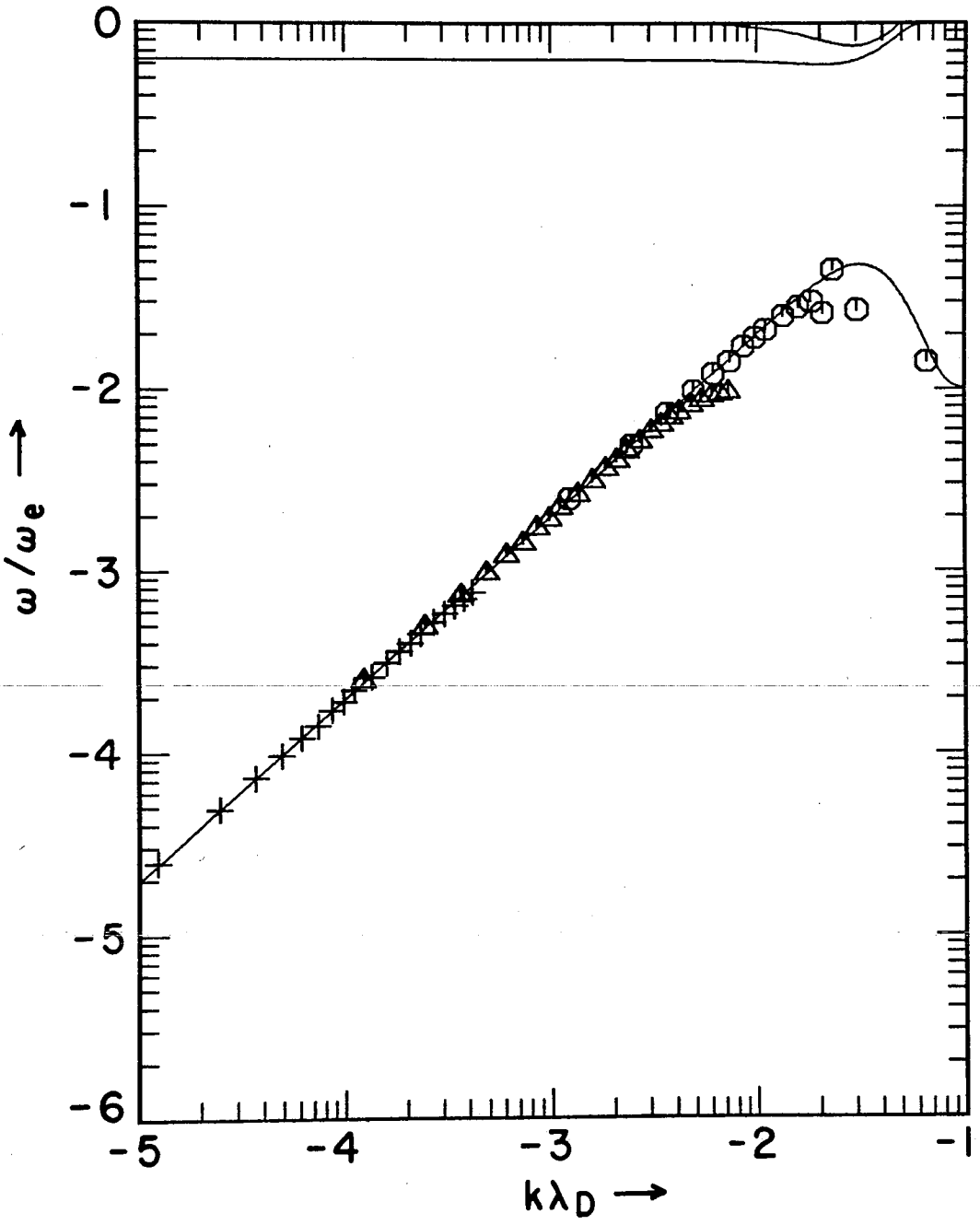

Figure 4

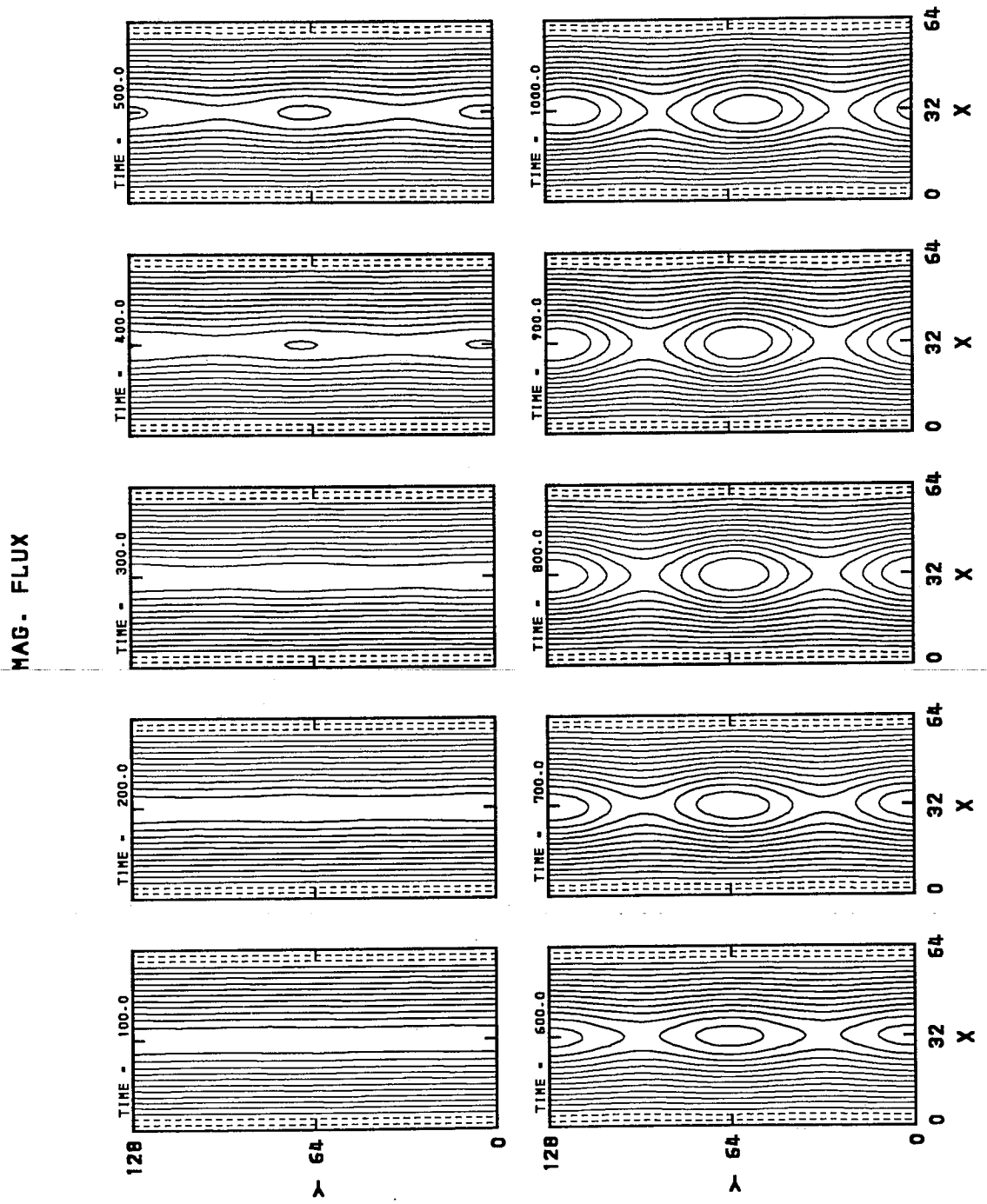
MAG. FLUX
TIME = 100.0
TIME = 200.0
TIME = 300.0
TIME = 400.0
TIME = 500.0
TIME = 600.0
TIME = 700.0
TIME = 800.0
TIME = 900.0
TIME = 1000.0
128
64
0
Y
0
32
64
X

Figure 5

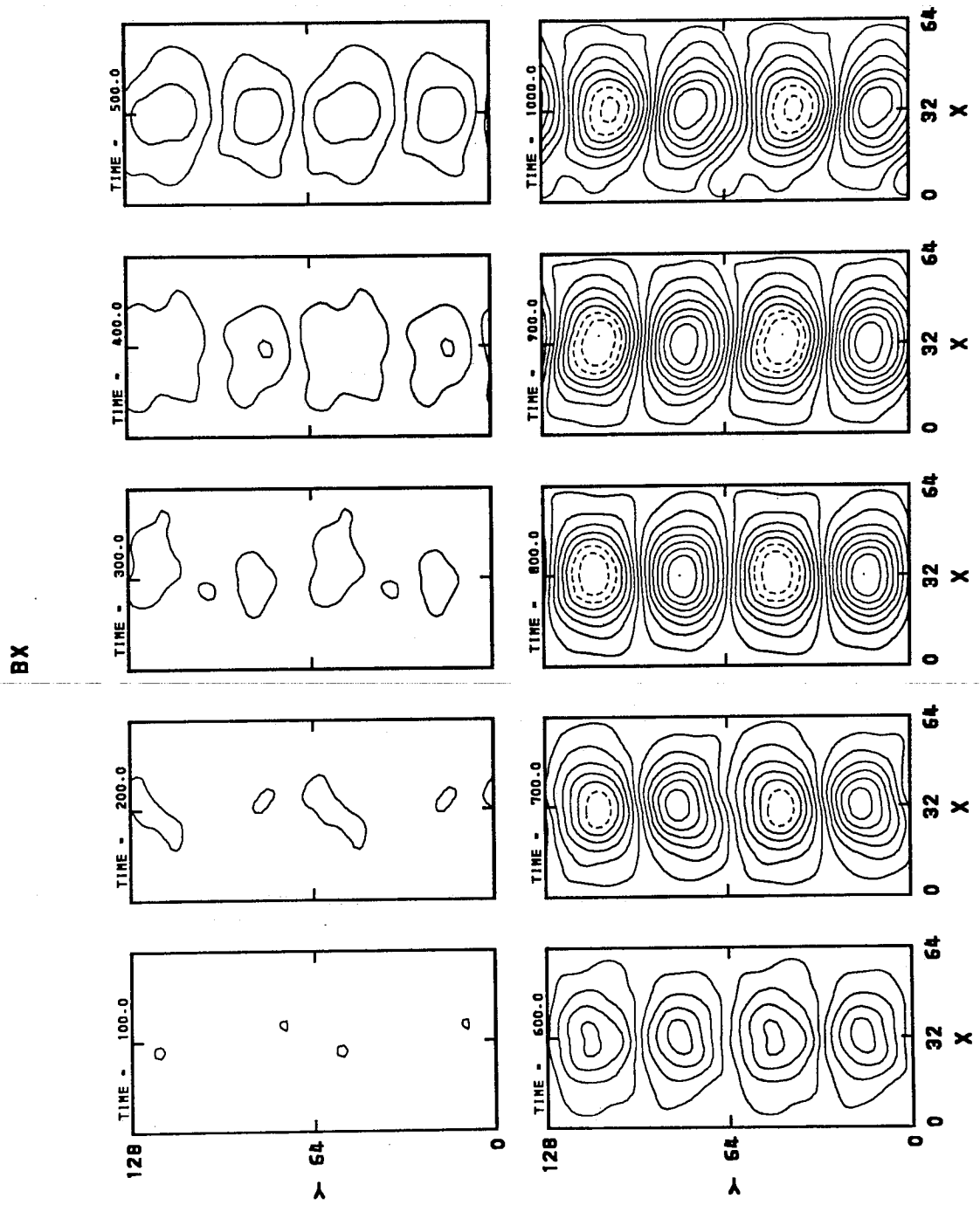
BX
TIME = 100.0
TIME = 200.0
TIME = 300.0
TIME = 400.0
TIME = 500.0
TIME = 600.0
TIME = 700.0
TIME = 800.0
TIME = 900.0
TIME = 1000.0
128
64
0
Y
0
32
64
X

Figure 6

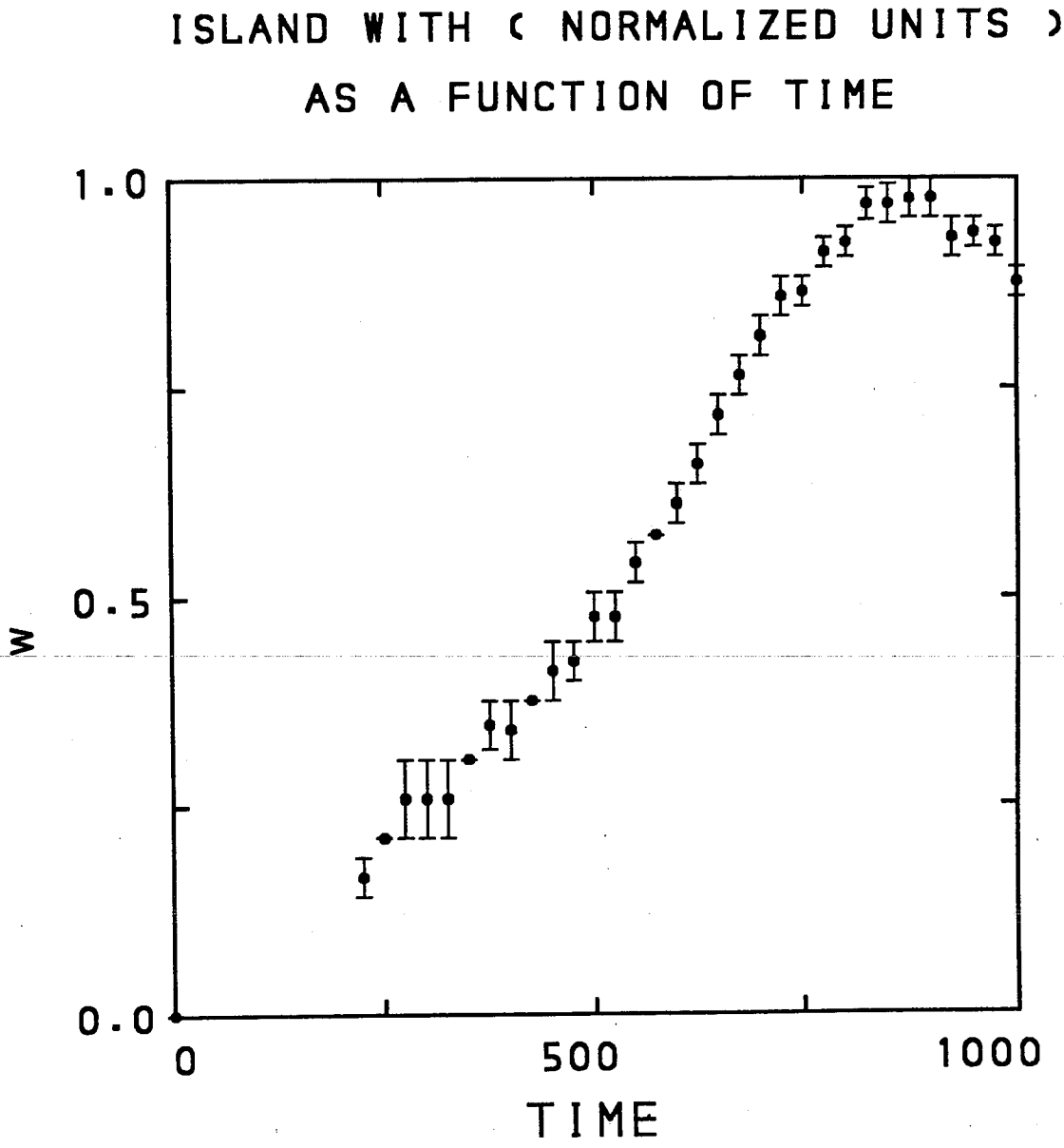
ISLAND WITH (NORMALIZED UNITS)
AS A FUNCTION OF TIME
1.0
0.5
0.0
W
0
500
1000
TIME

Figure 7

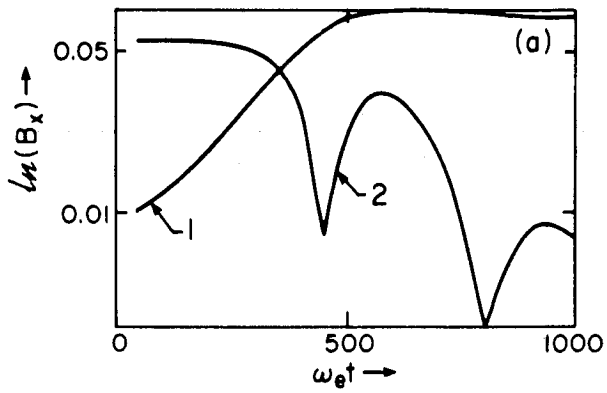
(a)
0.05
0.01
$\ln(B_x)$ →
1
2
0
500
1000
$\omega_e t$ →

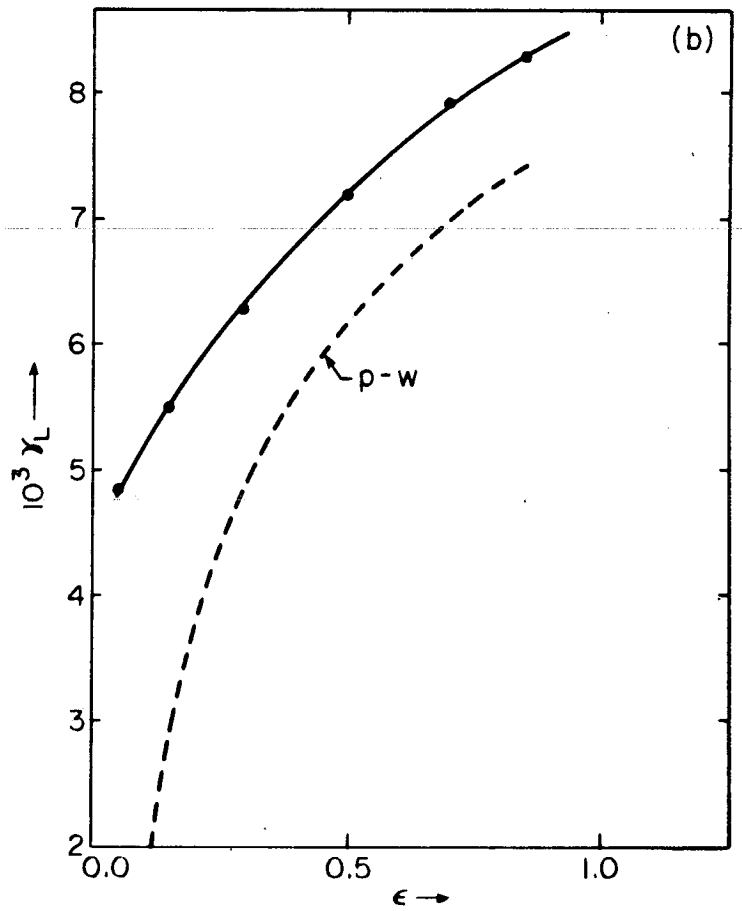
(b)
8
7
6
5
4
3
2
$10^3 \gamma_L$ →
p-w
0.0
0.5
1.0
ϵ →

Figure 8